Tellurium nanosheets with structural anisotropy formed from defective MoTe₂ multilayers

Shuto Muranaka ; Satoshi Nogamida; Kosuke O. Hara ; Kentarou Sawano ; Yusuke Hoshi ✉

Check for updates

View Online   Export Citation

Tellurium nanosheets with structural anisotropy formed from defective MoTe₂ multilayers

View Online Export Citation CrossMark

Shuto Muranaka,[1] [ID] Satoshi Nogamida,[1] Kosuke O. Hara,[2] [ID] Kentarou Sawano,[1] [ID] and Yusuke Hoshi[1,a)] [ID]

AFFILIATIONS

[1] Advanced Research Laboratories, Tokyo City University, 1-28-1 Tamazutsumi, Setagaya-ku, Tokyo 158-8557, Japan
[2] Center for Crystal Science and Technology, University of Yamanashi, Kofu, Yamanashi 400-8511, Japan

[a)]Author to whom correspondence should be addressed: yhoshi@tcu.ac.jp

ABSTRACT

We report on the formation of a tellurium nanosheet with a MoO_x cap by thermal annealing of ion-implanted 2H–MoTe₂ multilayers. The presence of crystal defects generated by ion implantation at an energy of 90 keV accelerates the incorporation of O atoms and the surface desorption of Te atoms in the defective MoTe₂ during thermal annealing, and subsequently, a tellurium nanosheet is formed around the bottom regions in the defective MoTe₂ due to tellurium segregation. For the angle-resolved Raman spectroscopy, polar plots exhibit two-fold and four-fold symmetries for peak intensities of 121 and 143 cm^{-1}, respectively, signifying the structural anisotropy of the tellurium nanosheet. On reducing the ion energy, the two Raman peak intensities collected from the tellurium nanosheet remarkably decrease, and they disappear for the sample at 30 keV. On the other hand, the decrease of the implantation energy increases the E_{2g} peak intensity at 235 cm^{-1}, which corresponds to the in-plane vibration mode of 2H–MoTe₂. The distribution of crystal defects along the depth direction tuned by ion implantation energy is very critical for the formation of a tellurium nanosheet with structural anisotropy from the 2H–MoTe₂ multilayers.

Transition metal dichalcogenides (TMDs) of MX₂ stoichiometry (M = Mo, W and X = S, Se, Te) exhibit diverse polymorphisms and exceptional optoelectronic properties.[1–3] Due to their unique physical properties of spatial inversion symmetry breaking and strong spin–orbit coupling, they have attracted considerable attention in the fields of electronics and photonics, taking advantage of valley polarization.[4–6] Recently, molybdenum ditelluride (MoTe₂) crystals have been considered a promising material for near-infrared optoelectronic devices and ambipolar channel FETs.[7–10] However, device performance is limited by the relatively high contact resistance. On the other hand, the MoTe₂ crystal is easily phase-engineered due to the small formation energy differences between the semiconducting 2H phase and the semi-metallic 1T′ phase. The 2H/1T′ MoTe₂ heterojunction has been reported to provide lower contact resistance than the 2H–MoTe₂/metal junction, owing to the suppression of Fermi level pinning.[11–13] Thus, techniques for phase engineering are highly expected to pave the way for improving the performances of electronic devices based on MoTe₂. Various techniques have been employed to induce the phase transition of the MoTe₂ crystals, including electrostatic

gating,[14] strain introduction,[15,16] and controlled chemical vapor deposition.[3,11,12,17,18] Optically induced electronic excitation in 2H–MoTe₂ crystals is also theoretically predicted to result in the structural phase transition due to the band structure control of monolayer MoTe₂.[19,20] However, experimental studies of the phase transition to 1T′-phase by laser irradiation remain controversial. It is thought that tellurium atoms segregate from MoTe₂ crystals due to the complexity of the strain effect, originating from the thermal expansion and Te vacancy formation.[13,21,22] Thus, it is very crucial to independently control the lattice temperature and defect distribution for the understanding of the structural transformation of 2H–MoTe₂ crystals.

Ion implantation is a traditional technique for doping ions into semiconductors, which is widely adopted in industrial electrical device processes. It can also intentionally create crystal defects using inert gas ions, and the defect depth and density are arbitrarily tuned by controlling the ion energy and dose. Implantation damages have been positively and extensively utilized for wafer splitting,[23] impurity gettering,[24] and strain engineering[25,26] in the fields of three-dimensional semiconductors. Therefore, it can be expected

that ion implantation is also helpful for a structural transformation based on crystal defect formation in two-dimensional materials. Here, we focus on the formation of a tellurium nanosheet with a MoO_x cap by a coupling of ion implantation with post-anneal for $MoTe_2$ multilayers. It is found that the tellurium nanosheet with structural anisotropy is formed due to tellurium segregation around the bottom regions of the defective $MoTe_2$. It is demonstrated that the defective $MoTe_2$ thickness induced by ion implantation can be tuned by ion implantation energy, which is critical for the formation of a tellurium nanosheet with structural anisotropy.

The sample fabrication process is summarized in Fig. 1(a). First, $2H–MoTe_2$ multilayers were mechanically exfoliated from bulk crystals onto a highly doped Si substrate with 280 nm-thick SiO_2 (Sample A). We then performed thermal treatment at $200\,^\circ C$ for 15 min and UV/O_3 cleaning to remove residues on the surface of the flakes. Ar ions were implanted into the $2H–MoTe_2$ multilayers at an ion dose of 5×10^{11} cm^{-2} and an energy of 30–90 keV. Subsequently, the implanted $2H–MoTe_2$ flakes were thermally annealed at $400\,^\circ C$ for 1 h in an atmosphere (Sample B). To measure the electrical properties, Ti/Au electrodes were evaporated on the surface using a standard lift-off process. As a reference, we prepared an as-implanted sample (Sample C) and a sample structure without ion implantation (Sample D).

A standard confocal microscope with a focusing diameter of $\sim2\,\mu m$ was used to measure the Raman spectra and mapping images. These measurements were carried out in an atmosphere at room temperature using a continuous-wave excitation laser emitting at 532 nm for spectral measurements and at 514.5 nm for mapping image measurements coupled to a 100× microscope objective. For measurements of angle-resolved Raman spectra, a linear polarizer was set in front of the spectrometer to polarize reflected light in the same direction as the incident light. By rotating the flakes, we observed angle-dependent Raman evolution. The Raman peak intensities of different vibration modes were extracted by fitting them with multiple Lorentz functions. To avoid undesirable thermal effects, the laser power was kept at 0.6 mW in these measurements.

Figure 1(b) shows the Raman spectra of samples A–D in a wavenumber range of 100–270 cm^{-1}. For the pristine sample (Sample A), the Raman spectrum is dominated by an in-plane vibration mode labeled as E_{2g} around 235 cm^{-1}, which is typical for 2H-phase $MoTe_2$ crystals. In contrast, two strong peaks at 121 and 143 cm^{-1} are clearly observed for sample B, which is fabricated by thermally annealing $MoTe_2$ with ion implantation at 90 keV. The Raman spectrum is quite similar to those of tellurium thin films formed by laser irradiation of $2H–MoTe_2$.[21] Thus, for sample B, tellurium layers should be formed owing to the combination of crystal defect formation by ion implantation with the incremental lattice temperature during thermal annealing. Note that the Raman signals attributed to the tellurium formation cannot be seen for samples C and D with either the ion implantation process or the thermal annealing process. It was also confirmed by scanning electron microscopy energy dispersive x-ray spectroscopy (SEM-EDX) that Ar ions incorporated into the $MoTe_2$ crystal by ion implantation were removed by thermal annealing. Therefore, crystal defects induced by ion implantation rather than the presence of Ar ions assist in the formation of the tellurium layers by thermal annealing. Figure 1(c) shows an atomic force microscope (AFM) image of sample B. The cross-sectional heights of the samples before and after thermal annealing at $400\,^\circ C$ reveal a reduction in the $MoTe_2$ thickness of $\sim$30–50 nm. Generally, bare $MoTe_2$ crystals lead to surface oxidation and crystal quality degradation by thermal annealing at more than $200\,^\circ C$.[27–29] Thus, the reduction in the $MoTe_2$ thickness should be attributed to the surface desorption of $MoTe_2$ crystals assisted by oxidation. Indeed, the amount of thickness reduction by the thermal anneal is almost the same as that of sample D without ion implantation. Notably, only for sample B, the tellurium layer remains even after the removal of the surface regions by thermal annealing. Figure 1(d) shows a spatial distribution of the integrated intensity of the Raman signals from the tellurium layers at $\sim$100–150 cm^{-1} for sample B. The Raman signals are observed over the entire area in the flake, and the intensity in Area II is clearly larger than that in Area I. In general, Raman intensity strongly depends on the crystal quality and
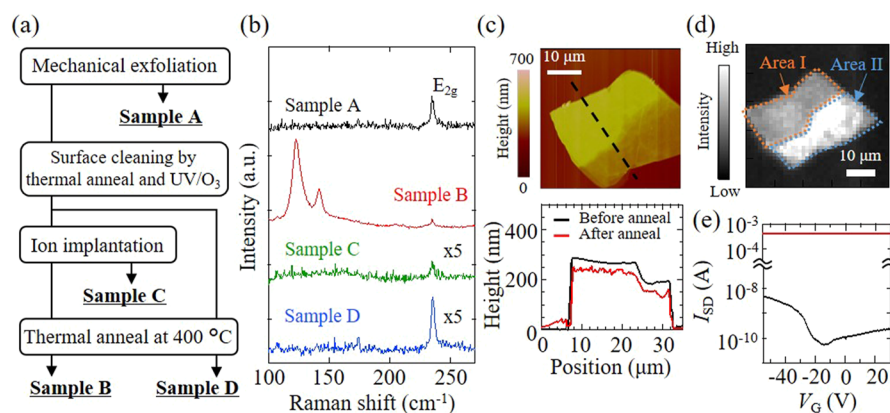
FIG. 1. (a) Sample fabrication process and (b) Raman spectra for an as-exfoliated $MoTe_2$ (sample A), a sample with both the ion implantation at 90 keV and the thermal anneal (sample B), only with the ion implantation (sample C), and only with the thermal anneal (sample D). (c) AFM image of sample B fabricated by the ion implantation at 90 keV. Cross-sectional height profiles for the sample before (black) and after (red) the thermal anneal along the black dashed line in the AFM image. (d) Raman intensity maps of the two peaks attributed to the tellurium around 100–150 cm^{-1} for sample B. (e) $I_{SD}–V_G$ curves for sample A (black) and sample B (red) with UV/O_3 cleaning.

thickness of the materials. Considering the smaller thickness in Area II, the larger Raman intensities might result from the better quality of the tellurium layers. To verify that the tellurium nanosheet has high conductivity, we measured the current–voltage characteristics of the two-terminal device structures after the UV/O_3 cleaning of sample surfaces. For the conventional 2H-phase $MoTe_2$ channel device, ambipolar transport behavior can be observed by applying a back-gate voltage V_G. In contrast, the device structure with the tellurium nanosheet showed V_G-independent transport behavior, demonstrating the formation of highly conductive materials by the thermal annealing of the ion-implanted $MoTe_2$ crystal.

Figure 2(a) shows the cross-sectional image of the high-angle annular dark field scanning transmission electron microscopy (HAADF-STEM) for the sample structure implanted at an energy of 90 keV. Contrast fluctuations are observed at a depth of ~120–170 nm, with uniformly distributed bright regions located at depths below 170 nm. Figures 2(b)–2(d) display the STEM-EDX elemental maps for (b) Mo, (c) Te, and (d) O within the same region shown in Fig. 2(a). Mo signals are detectable at the depth ranging from the surface to 250 nm, except for the depth region around 150 nm. Te signals are notably prominent in the regions deeper than 120 nm. Intriguingly, only Te signals are observed in the regions where Mo and O signals are absent around a depth of 150 nm, indicating the formation of pure tellurium nanosheets. From the stopping and range of ions in matter (SRIM) simulation result, we can estimate the defect depth in the $MoTe_2$ crystals generated by Ar ion implantation at 90 keV. Mo and Te atoms from the surface to a 170 nm-depth are recoiled due to the Ar ion implantation at 90 keV. The distribution of recoiled densities (RD) of Mo and Te atoms is very consistent with the depth where the O signals are distributed, indicating the formation of the defective $MoTe_2$ with 170 nm thickness by the ion implantation. The mechanism for the tellurium nanosheet formation is as follows:[1] Ar ion implantation breaks the covalent bonds between Mo and Te atoms in 2H–$MoTe_2$ and forms the defective $MoTe_2$ in the ion-implanted region.[2] During thermal annealing in air, the incorporation of the O atoms is

accelerated by the existence of the crystal defects. The Mo atoms in the defective region are predominantly oxidized, and consequently, the crystal structure of $MoTe_2$ cannot be maintained after thermal annealing.[3] Te atoms are segregated around the interface between the top defective region and the bottom single-crystal region in the 2H–$MoTe_2$ during the thermal annealing. Indeed, the contrast between Te and O signals seems to be reversed in the region from the surface to 170 nm depth. It can also be confirmed that the Mo concentration is slightly higher around the tellurium nanosheets owing to the exclusion of Mo atoms attributed to the Te segregation. The Mo and Te ratio is almost 1:2 in the depth below 170 nm without the crystal defects based on the ion implantation, and oxygen atoms are not incorporated into the region.

To investigate the crystal structure of the tellurium nanosheets, we measured the angle-resolved Raman spectra for the sample implanted with an energy of 90 keV. By rotating the sample in steps of $15°$, we observed the changes in the angle-resolved Raman spectral shape [Fig. 3(a)]. The Raman spectra of the sample exhibit two main Raman-active phonon modes at 121 and 143 cm^{-1}. Figures 3(b) and 3(c) show polar plots for the peak intensities of these modes, obtained by fitting with the Lorentz function. The polar plots for the 121 cm^{-1} peak maximize at $90°$ and $270°$, while the peak from 143 cm^{-1} shows four-fold symmetry. These changes in the polar plots result from structural anisotropy of the tellurium nanosheet formed by thermal annealing of the defective $MoTe_2$ multilayer, suggesting the formation of a two-dimensional tellurene. The tellurene has a crystal structure in which a chiral-chain crystal lattice extends along the [0001] direction and couples relatively weakly with each other to form 2D-like sheets. The wavenumbers of the Raman peaks obtained from the sample agree well with those of the tellurene, where the Raman peaks of 121 and 143 cm^{-1}
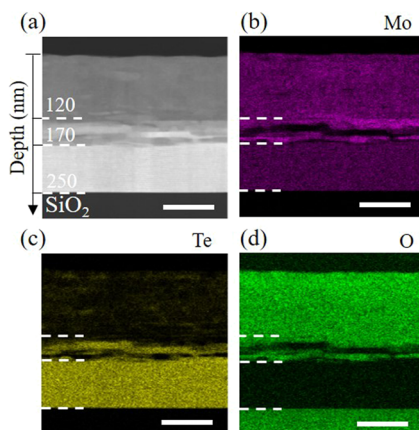

FIG. 2. (a) Cross-sectional HAADF STEM image of the sample fabricated by thermal annealing of the ion-implanted $MoTe_2$ multilayers. Cross-sectional STEM-EDX maps showing the spatial distribution of (b) Mo, (c) Te, and (d) O atoms. The scale bar is 100 nm for all figures.
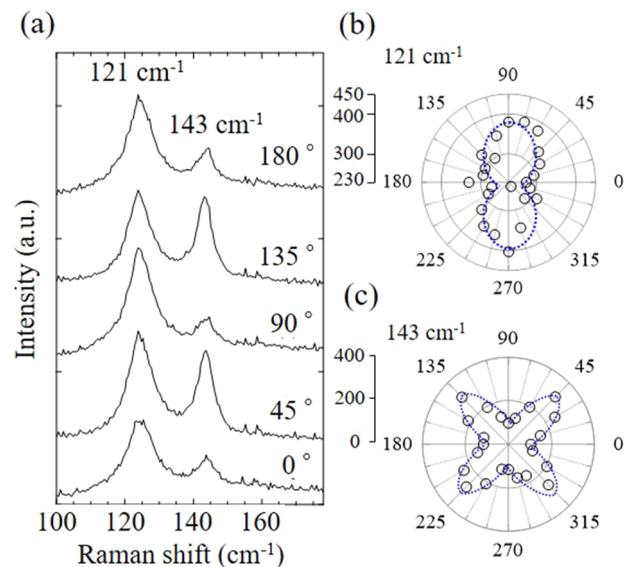

FIG. 3. Angle-resolved Raman spectra for the tellurium nanosheet fabricated by thermal annealing of the ion-implanted $MoTe_2$ multilayers. (a) Evolution with angles between crystal orientation and incident laser polarization. Polar figures of Raman peak intensity located at (b) 121 cm^{-1} and (c) 143 cm^{-1}.
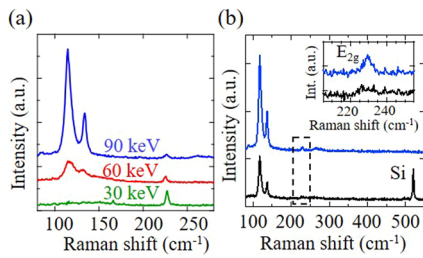
FIG. 4. (a) Raman spectra for sample structures fabricated by ion implantation of energy at 30 (green), 60 (red), and 90 keV (blue). (b) Raman spectra for the sample structures fabricated from the different initial $MoTe_2$ thicknesses of 110 nm (black) and 200 nm (blue). Ion implantation energy is fixed at 90 keV. The spectra enlarged in the region surrounded by a black dashed line are represented in the inset.

correspond to chain expansion mode in which each atom moves in the basal plane (A_1 mode) and asymmetric stretching mode mainly along the [0001] helical chain direction (E_2 mode), respectively.[30–32] As seen in Fig. 2(c), the Te atoms seem to slightly remain at the cap layer ranging from the surface to the 120 nm depth after the thermal annealing. Since the O atoms are uniformly distributed in the region, not only MoO_x but also TeO_x might be formed in the cap layer. Previous studies have shown that Raman peaks emerge around 120 and 145 cm^{-1} for tellurium oxide complexes.[33,34] However, it is thought that the Raman signals dominantly come from the tellurium nanosheet around the 150 nm depth since the Raman peaks obtained from the tellurium oxide complexes do not possess any anisotropic response.

Figure 4(a) shows the Raman spectra of the samples obtained from 190–200 nm thick 2H–$MoTe_2$ flakes implanted at 30, 60, and 90 keV. Upon reducing the implantation energy, the two Raman peak intensities of 121 and 143 cm^{-1} collected from the tellurium nanosheet remarkably decrease, and they disappear for the sample at 30 keV. In addition, it is found that the decrease of the implantation energy increases the E_{2g} peak intensity at 235 cm^{-1}, which corresponds to the in-plane vibration mode of 2H–$MoTe_2$. As mentioned above, the defect depth in the $MoTe_2$ bulk crystals generated by Ar ion implantation at 90 keV is estimated to be around 170 nm from the SRIM simulation result. In contrast, the RD of Mo and Te atoms at 30 keV is distributed around a depth of 70 nm from the surface. Considering the surface desorption during thermal annealing, the smaller ion implantation energy leads to the removal of the defective $MoTe_2$ region without tellurium segregation, and the deeper 2H–$MoTe_2$ region remains after thermal annealing. Figure 4(b) shows the Raman spectra of the samples fabricated from different initial $MoTe_2$ thicknesses of 110 and 200 nm with ion implantation at 90 keV. The Raman signals attributed to the tellurium nanosheet formation are observed for both samples although the E_{2g} peak of the 2H phase is not observed for the sample with a thinner initial thickness, as shown in the inset of Fig. 4(b). Moreover, for the sample with a thinner initial thickness, the Raman peak from the Si substrate is clearly observed at 521 cm^{-1}, showing that the 2H–$MoTe_2$, which absorbs optical signals from the Si substrate, does not exist. This is a direct observation of the tellurium nanosheet formation without the bottom 2H–$MoTe_2$ layer by tuning the defective $MoTe_2$ region. The initial 2H–$MoTe_2$ thickness of 110 nm is smaller than the projected

range of ion implantation at 90 keV, and thus, the existence of the bottom 2H–$MoTe_2$ is not crucial for the tellurium nanosheet formation. Considering the thermal annealing at a lower temperature compared to that of Te diffusion in SiO_2, the tellurium nanosheet should be formed around the interface between the defective layer and SiO_2.[35]

Tellurium segregation in the deeper region of the 2H–$MoTe_2$ is achieved through a combination of thermal annealing in air and the formation of crystal defects by ion implantation. We confirmed that laser irradiation of 2H–$MoTe_2$ in an atmospheric environment leads to the emergence of Raman signals associated with tellurium formation (not shown), which is consistent with the previous report.[36,37] In contrast, it has been reported that laser irradiation of hBN-encapsulated $MoTe_2$ induces a phase transition. Therefore, it can be concluded that the oxidation of 2H–$MoTe_2$ by thermal annealing in the air plays an important role in the tellurium nanosheet formation.

In summary, we demonstrated the formation of tellurium nanosheets with MoO_x caps by the thermal annealing of ion-implanted $MoTe_2$ multilayers. Crystal defects were induced by ion implantation in the $MoTe_2$ multilayers, and thermal decomposition by annealing the crystals enabled the formation of the tellurium nanosheet with structural anisotropy from the 2H–$MoTe_2$. For the ion implanted sample at more than 60 keV, the tellurium nanosheet was formed in the entire area of the flakes, while at 30 keV, it disappeared due to surface desorption of the $MoTe_2$ crystals during thermal annealing at 400 °C. At an implantation energy of 90 keV, the sample fabricated from the 200 nm thick $MoTe_2$ possessed 2H-phase $MoTe_2$ under the tellurium nanosheet, whereas only the tellurium nanosheet with a MoO_x cap was formed by utilizing $MoTe_2$ with an initial thickness of ~110 nm. It can be concluded that the distribution of the crystal defects induced in the 2H–$MoTe_2$ crystal is crucial for the formation of the tellurium nanosheet.

AUTHOR DECLARATIONS

Conflict of Interest

The authors have no conflicts to disclose.

Author Contributions

Shuto Muranaka: Data curation (equal); Formal analysis (equal); Investigation (lead); Validation (equal); Visualization (equal); Writing – original draft (lead). **Satoshi Nogamida**: Data curation (supporting); Formal analysis (equal); Investigation (equal); Methodology (supporting); Visualization (supporting). **Kosuke O. Hara**: Investigation (supporting); Methodology (supporting); Writing – review & editing (supporting). **Kentarou Sawano**: Funding acquisition (equal); Methodology (supporting); Supervision (supporting); Writing – review & editing (supporting). **Yusuke Hoshi**: Conceptualization (lead); Data curation (equal); Formal analysis (equal); Funding acquisition (equal); Investigation (equal); Methodology (lead); Project administration (lead);

Resources (equal); Software (equal); Supervision (lead); Validation (lead); Visualization (supporting); Writing – original draft (supporting); Writing – review & editing (lead).

DATA AVAILABILITY

The data that support the findings of this study are available from the corresponding author upon reasonable request.

REFERENCES

[1] K.-A. N. Duerloo, Y. Li, and E. J. Reed, Nat. Commun. **5**, 4214 (2014).

[2] D. H. Keum, S. Cho, J. H. Kim, D.-H. Choe, H.-J. Sung, M. Kan, H. Kang, J.-Y. Hwang, S. W. Kim, H. Yang, K. J. Chang, and Y. H. Lee, Nat. Phys. **11**, 482 (2015).

[3] T. A. Empante, Y. Zhou, V. Klee, A. E. Nguyen, I.-H. Lu, M. D. Valentin, S. A. Naghibi Alvillar, E. Preciado, A. J. Berges, C. S. Merida, M. Gomez, S. Bobek, M. Isarraraz, E. J. Reed, and L. Bartels, ACS Nano **11**, 900 (2017).

[4] H. Zeng, J. Dai, W. Yao, D. Xiao, and X. Cui, Nat. Nanotechnol. **7**, 490 (2012).

[5] K. F. Mak, K. He, J. Shan, and T. F. Heinz, Nat. Nanotechnol. **7**, 494 (2012).

[6] J. Qi, X. Li, Q. Niu, and J. Feng, Phys. Rev. B **92**, 121403 (2015).

[7] Y.-Q. Bie, G. Grosso, M. Heuck, M. M. Furchi, Y. Cao, J. Zheng, D. Bunandar, E. Navarro-Moratalla, L. Zhou, D. K. Efetov, T. Taniguchi, K. Watanabe, J. Kong, D. Englund, and P. Jarillo-Herrero, Nat. Nanotechnol. **12**, 1124 (2017).

[8] S. Li, Z. He, Y. Ke, J. Guo, T. Cheng, T. Gong, Y. Lin, Z. Liu, W. Huang, and X. Zhang, Appl. Phys. Express **13**, 015007 (2020).

[9] Y.-F. Lin, Y. Xu, S.-T. Wang, S.-L. Li, M. Yamamoto, A. Aparecido-Ferreira, W. Li, H. Sun, S. Nakaharai, W.-B. Jian, K. Ueno, and K. Tsukagoshi, Adv. Mater. **26**, 3263 (2014).

[10] H. Huang, J. Wang, W. Hu, L. Liao, P. Wang, X. Wang, F. Gong, Y. Chen, G. Wu, W. Luo, H. Shen, T. Lin, J. Sun, X. Meng, X. Chen, and J. Chu, Nanotechnology **27**, 445201 (2016).

[11] X. Zhang, Z. Jin, L. Wang, J. A. Hachtel, E. Villarreal, Z. Wang, T. Ha, Y. Nakanishi, C. S. Tiwary, J. Lai, L. Dong, J. Yang, R. Vajtai, E. Ringe, J. C. Idrobo, B. I. Yakobson, J. Lou, V. Gambin, R. Koltun, and P. M. Ajayan, ACS Appl. Mater. Interfaces **11**, 12777 (2019).

[12] R. Ma, H. Zhang, Y. Yoo, Z. P. Degregorio, L. Jin, P. Golani, J. Ghasemi Azadani, T. Low, J. E. Johns, L. A. Bendersky, A. V. Davydov, and S. J. Koester, ACS Nano **13**, 8035 (2019).

[13] S. Cho, S. Kim, J. H. Kim, J. Zhao, J. Seok, D. H. Keum, J. Baik, D.-H. Choe, K. J. Chang, K. Suenaga, S. W. Kim, Y. H. Lee, and H. Yang, Science **349**, 625 (2015).

[14] Y. Wang, J. Xiao, H. Zhu, Y. Li, Y. Alsaid, K. Y. Fong, Y. Zhou, S. Wang, W. Shi, Y. Wang, A. Zettl, E. J. Reed, and X. Zhang, Nature **550**, 487 (2017).

[15] S. Song, D. H. Keum, S. Cho, D. Perello, Y. Kim, and Y. H. Lee, Nano Lett. **16**, 188 (2016).

[16] H. H. Huang, X. Fan, D. J. Singh, H. Chen, Q. Jiang, and W. T. Zheng, Phys. Chem. Chem. Phys. **18**, 4086 (2016).

[17] T. Kim, H. Park, D. Joung, D. Kim, R. Lee, C. H. Shin, M. Diware, W. Chegal, S. H. Jeong, J. C. Shin, J. Park, and S.-W. Kang, Adv. Mater. Interfaces **5**, 1800439 (2018).

[18] C. Martella, A. Quadrelli, P. P. Tummala, C. Lenardi, R. Mantovan, A. Lamperti, and A. Molle, Cryst. Growth Des. **21**, 2970 (2021).

[19] A. V. Kolobov, P. Fons, and J. Tominaga, Phys. Rev. B **94**, 094114 (2016).

[20] B. Peng, H. Zhang, W. Chen, B. Hou, Z.-J. Qiu, H. Shao, H. Zhu, B. Monserrat, D. Fu, H. Weng, and C. M. Soukoulis, npj 2D Mater. Appl. **4**, 14 (2020).

[21] K. Sakanashi, H. Ouchi, K. Kamiya, P. Krüger, K. Miyamoto, T. Omatsu, K. Ueno, K. Watanabe, T. Taniguchi, J. P. Bird, and N. Aoki, Nanotechnology **31**, 205205 (2020).

[22] T. Fukuda, R. Kaburauchi, Y. Saito, K. Makino, P. Fons, K. Ueno, and M. Hase, Phys. Status Solidi RRL **16**, 2100633 (2022).

[23] M. Bruel, B. Aspar, and J. Auberton-Herve, Jpn. J. Appl. Phys. **36**, 1636 (1997).

[24] R. A. Brown, O. Kononchuk, G. A. Rozgonyi, S. Koveshnikov, A. P. Knights, P. J. Simpson, and F. González, J. Appl. Phys. **84**, 2459 (1998).

[25] K. Sawano, A. Fukumoto, Y. Hoshi, J. Yamanaka, K. Nakagawa, and Y. Shiraki, Thin Solid Films **517**, 87 (2008).

[26] Y. Hoshi, K. Sawano, A. Yamada, N. Usami, K. Arimoto, K. Nakagawa, and Y. Shiraki, J. Appl. Phys. **107**, 103509 (2010).

[27] H. Zhu, Q. Wang, L. Cheng, R. Addou, J. Kim, M. J. Kim, and R. M. Wallace, ACS Nano **11**, 11005 (2017).

[28] F. Ahmed, A. M. Shafi, D. M. A. Mackenzie, M. A. Qureshi, H. A. Fernandez, H. H. Yoon, M. G. Uddin, M. Kuittinen, Z. Sun, and H. Lipsanen, Adv. Mater. Interfaces **8**, 2100950 (2021).

[29] S. Hayashida, R. Saitoh, K. Watanabe, T. Taniguchi, K. Sawano, and Y. Hoshi, ACS Appl. Electron. Mater. **2**, 2739 (2020).

[30] Y. Wang, G. Qiu, R. Wang, S. Huang, Q. Wang, Y. Liu, Y. Du, W. A. Goddard, M. J. Kim, X. Xu, P. D. Ye, and W. Wu, Nat. Electron. **1**, 228 (2018).

[31] S. Yang, B. Chen, Y. Qin, Y. Zhou, L. Liu, M. Durso, H. Zhuang, Y. Shen, and S. Tongay, Phys. Rev. Mater. **2**, 104002 (2018).

[32] A. Apte, E. Bianco, A. Krishnamoorthy, S. Yazdi, R. Rao, N. Glavin, H. Kumazoe, V. Varshney, A. Roy, F. Shimojo, E. Einge, R. K. Kalia, A. Nakano, C. S. Tiwary, P. Vashishta, V. Kochat, and P. M. Ajayan, 2D Mater. **6**, 015013 (2019).

[33] S. Yang, H. Cai, B. Chen, C. Ko, V. O. Özçelik, D. F. Ogletree, C. E. White, Y. Shen, and S. Tongay, Nanoscale **9**, 12288 (2017).

[34] J. Kopaczek, K. Yumigeta, A. Ibrahim, M. Y. Sayyad, S. Sinha, R. Sailus, P. Hays, S. T. R. Moosavy, S. Susarla, C. Ataca, R. Kudrawiec, and S. Tongay, Adv. Electron. Mater. **9**, 2201129 (2023).

[35] P. B. Dayal, B. R. Mehta, Y. Aparna, and S. M. Shivaprasad, Appl. Phys. Lett. **81**, 4254 (2002).

[36] H. Ryu, J. Lee, H. J. Kim, S. H. Kang, Y. Kang, K. Kim, J. Kim, B. E. Janicek, K. Watanabe, T. Taniguchi, P. Y. Huang, H. Cheong, I. H. Jung, K. Kim, Y. W. Son, and G. H. Lee, Adv. Funct. Mater. **31**, 2107376 (2021).

[37] C.-H. Lee, H. Ryu, G. Nolan, Y. Zhang, Y. Lee, S. Oh, H. Cheong, K. Watanabe, T. Taniguchi, K. Kim, G.-H. Lee, and P. Y. Huang, Nano Lett. **23**, 677 (2023).